




# Sol–gel synthesis of iron titanates for the photocatalytic degradation of cyanide

Stefanny Córdoba-Miranda<sup>1</sup>, Ingrid C. Ortiz-Rojas<sup>1</sup>, Diana M. Cañas-Martínez<sup>1</sup>, Juvencio Vazquez-Samperio<sup>1,2</sup>, and Julio A. Pedraza-Avella<sup>1,\*</sup> 

<sup>1</sup> Grupo de Investigaciones en Minerales, Biohidrometalurgia y Ambiente - GIMBA, Universidad Industrial de Santander - UIS, Sede Guatiguará, Transv. Guatiguará, Calle 8N No. 3W-60, Barrio El Refugio, C.P. 681011 Piedecuesta, Santander, Colombia

<sup>2</sup> Laboratorio Nacional de Conversión y Almacenamiento de Energía, Instituto Politécnico Nacional, CICATA - Legaria, Calzada Legaría 694, Col. Irrigación, CDMX 11500, México

Received: 28 April 2024

Accepted: 24 June 2024

Published online:  
21 July 2024

© The Author(s), 2024

## ABSTRACT

Iron titanate mixed metal oxides were synthesized by the sol–gel method through four different routes. The effect of (i) the solvent of iron precursor, (ii) the addition of the chelating agent to the titanium or iron solution and (iii) the molar ratio between the chelating agent and the titanium or iron precursor over the overall percentage of obtained iron titanates was evaluated. Fourier-transform infrared spectroscopy (FTIR) and UV–Vis spectroscopy (UV–Vis) performed on the reaction medium evidenced the formation of acetate complexes of titanium (IV) or iron (III) during the different routes. X-ray diffraction (XRD) patterns of the obtained materials showed the formation of ilmenite (FeTiO<sub>3</sub>), pseudorutile (Fe<sub>2</sub>Ti<sub>3</sub>O<sub>9</sub>) and pseudobrookite (Fe<sub>2</sub>TiO<sub>5</sub>) in different proportions, as well as hematite (Fe<sub>2</sub>O<sub>3</sub>), rutile [TiO<sub>2</sub> (R)] and anatase [TiO<sub>2</sub> (A)]. The materials with the highest content of iron titanates obtained in each route were characterized and evaluated in the photocatalytic degradation of cyanide using visible light irradiation. UV–Vis Diffuse Reflectance Spectroscopy (UV–Vis DRS) showed that the samples exhibited energy bandgap values between 2.31 and 2.90 eV, which agrees with the values reported for iron titanates and evidence the possible activation of the materials under visible light. Scanning electron microscopy (SEM) and nitrogen physisorption results showed that the synthesized materials exhibited nanometric particle size and lower surface area ( $36.7 \pm 4.8 \text{ m}^2 \cdot \text{g}^{-1}$ ) than TiO<sub>2</sub> Degussa P-25 ( $72\text{--}155 \text{ m}^2 \cdot \text{g}^{-1}$ ). The photocatalytic performance of the synthesized materials toward oxidation of CN<sup>−</sup> exceeded by 56% the activity of pure TiO<sub>2</sub>. The content of iron titanates in the synthesized materials was found to be the variable with the greatest influence on the photodegradation of cyanide. In addition, an inversely

Handling Editor: M. Grant Norton.

Stefanny Córdoba-Miranda, Ingrid C. Ortiz-Rojas have contributed equally to this work and share first authorship.

Address correspondence to E-mail: apedraza@uis.edu.co

proportional relationship between the pseudorutile content of the materials and their photocatalytic activity was observed.

## Introduction

Titanium dioxide ( $\text{TiO}_2$ ) is a material of technological relevance that has been widely studied and used as a semiconductor in photocatalytic processes to degrade organic and inorganic pollutants [1–3]. However, as it is well known, the bandgap ( $E_g$ ) of  $\text{TiO}_2$  lies between 3.0 and 3.2 eV, which represents one of the major drawbacks for its application as a photocatalyst since its activation is limited to ultraviolet (UV) radiation, hindering the use of the solar radiation, compressed only by 3–5% UV radiation [4, 5]. Therefore, many investigations have focused on reducing the energy gap between the conduction and the valence band of  $\text{TiO}_2$  using different techniques, such as its doping with metallic ions like iron. The insertion of iron ions enables the decrease in the energy bandgap of  $\text{TiO}_2$  resulting in an enhanced photoactivity under visible light [6]. Considering this and owing to the inherent advantages of iron/titanium-containing oxides, several authors have devoted their efforts to the synthesis and evaluation of iron titanates; metallic oxides with a high content of iron and titanium in their crystalline structure provide the materials with excellent electrical, magnetic, and photocatalytic properties [7–14].

Among the most relevant iron titanates one can find ilmenite— $\text{FeTiO}_3$ , whose energy bandgap between 2.58 and 2.90 eV makes it a favorable semiconductor for photocatalytic applications, due to the possibility of activating it under the incidence of visible light radiation [15]. Other iron titanates of great interest are pseudobrookite— $\text{Fe}_2\text{TiO}_5$ , which has an orthorhombic crystal structure and is used in multiple areas including photocatalysis ( $E_g = 2.18$  eV), and pseudorutile— $\text{Fe}_2\text{Ti}_3\text{O}_9$ , which is important to analyze as a photocatalyst because it is a mineral intermediate between ilmenite and rutile ( $\text{TiO}_2$ ) [16, 17].

In the synthesis of ceramic nanomaterials, such as iron titanates, a wide variety of technologies have been used, including the sol–gel process, a soft chemical method characterized by being a relatively simple and highly efficient technique that grants the obtention of metastable phases, with low environmental impact and low energy requirements [18–20]. In 1939, the first research employing the sol–gel method for the preparation of oxide coatings was

reported [21]. Afterward, the process began to be investigated with greater interest by the scientific community, and in 1971, Dislich demonstrated that the use of alkoxides of various elements as precursors permits the synthesis of metal oxides and mixed oxide compounds with high homogeneity and purity [22]. The attractiveness of this advanced synthesis technique is that it enables the modification of the final properties of the material such as morphology, texture, and particle size, through the manipulation and control of the reactions that take place during the process (hydrolysis and condensation) [23–25].

In this research, the synthesis of iron titanate materials was carried out in the presence of a chelating agent, a compound capable of forming complexes with metal ions by the donation of electron pairs. These complexes (chelates) are more chemically stable, granting the control of the hydrolysis and polycondensation reactions kinetics and favoring the formation of compounds with a more homogeneous crystalline structure. The chelating force depends on different factors such as the physicochemical properties of the metal ions involved in the bond [26, 27]. Thus, the influence of the mixing order in the final properties of the material was evaluated by chelating both, the titanium and iron precursor solutions. Despite the multiple advantages that the chelation process offers, the kinetics of the reactions can also be affected by the amount of chelating agent present in the reaction medium. Thus, the chelating agent concentration was also evaluated in this research, and three different values were set, as reported in the literature by Guzmán, Ponmani and Chen [28–30]. The solvent of iron precursor was also varied to analyze its influence on the final properties of the materials, since the volume of the reaction medium may affect the interaction between the particles. Finally, the photocatalytic performance toward the degradation of  $\text{CN}^-$  was evaluated. Reaction mechanisms between the chelating agent and the precursors were proposed. Moreover, the formation of chelated compounds during the synthesis process and its influence on the sol–gel reactions stability were demonstrated. Materials, containing up to 70% iron titanates (ilmenite, pseudobrookite, and pseudorutile), were successfully synthesized and exhibited the

capability to degrade 14.38% of  $\text{CN}^-$  from a cyanide solution.

## Experimental

### Chemicals and reagents

Titanium (IV) butoxide [hereinafter ' $\text{Ti}(\text{OBU})_4$ '] (Sigma-Aldrich, 99% purity) and iron (III) chloride (hereinafter ' $\text{FeCl}_3$ ') (Merck, 99% purity) were used as metal precursors. Acetic acid (Merck, 99% purity) was used as chelating agent. Ethanol (hereinafter ' $\text{EtOH}$ ') (Merck, 99% purity) and de-ionized water were used as solvents. All the reagents were used as received from the supplier with no further treatment.

### Synthesis of the photocatalyst

With the aim of evaluating the effects of the presence and concentration of chelating agent, as well as the chelated metal ion (either Ti or Fe), four synthesis routes were designed as depicted in Fig. 1. The solvent of iron precursor was also varied to analyze its

influence on the final properties of the materials, as it may affect the interaction between the particles.

Attempting to favor the obtention of pseudorutile ( $\text{Fe}_2\text{Ti}_3\text{O}_9$ ), an iron/titanium (Fe/Ti) molar ratio of 1/3 was used to ensure higher titanium concentration in the resulting crystalline structure.

In Route I, a core solution 0.5 M of  $\text{Ti}(\text{OBU})_4$  was prepared using 15 mL of EtOH as solvent. Subsequently, acetic acid was added with molar ratio acetic acid/ $\text{Ti}(\text{OBU})_4$  of 1/1; 2/1 or 3/1. In every case, the corresponding amount of acetic acid was diluted in 15 mL of EtOH and this solution was quickly poured onto the core solution. To the resulting mixture, a solution of  $\text{FeCl}_3$  dissolved in 15 mL of EtOH was added dropwise, maintaining a molar ratio  $\text{FeCl}_3/\text{Ti}(\text{OBU})_4$  of 1/3. Lastly,  $\text{H}_2\text{O}$  was added in molar ratio  $\text{H}_2\text{O}/\text{Ti}(\text{OBU})_4$ : 4.

In Route II, the mixing order was the same as in Route I. However, instead of EtOH, the required stoichiometric amount of water [molar ratio  $\text{H}_2\text{O}/\text{Ti}(\text{OBU})_4$ : 4] was used as solvent of the  $\text{FeCl}_3$  solution. Thus, the volume of the overall sol was smaller in comparison with the previous route, affecting the interaction between the particles.

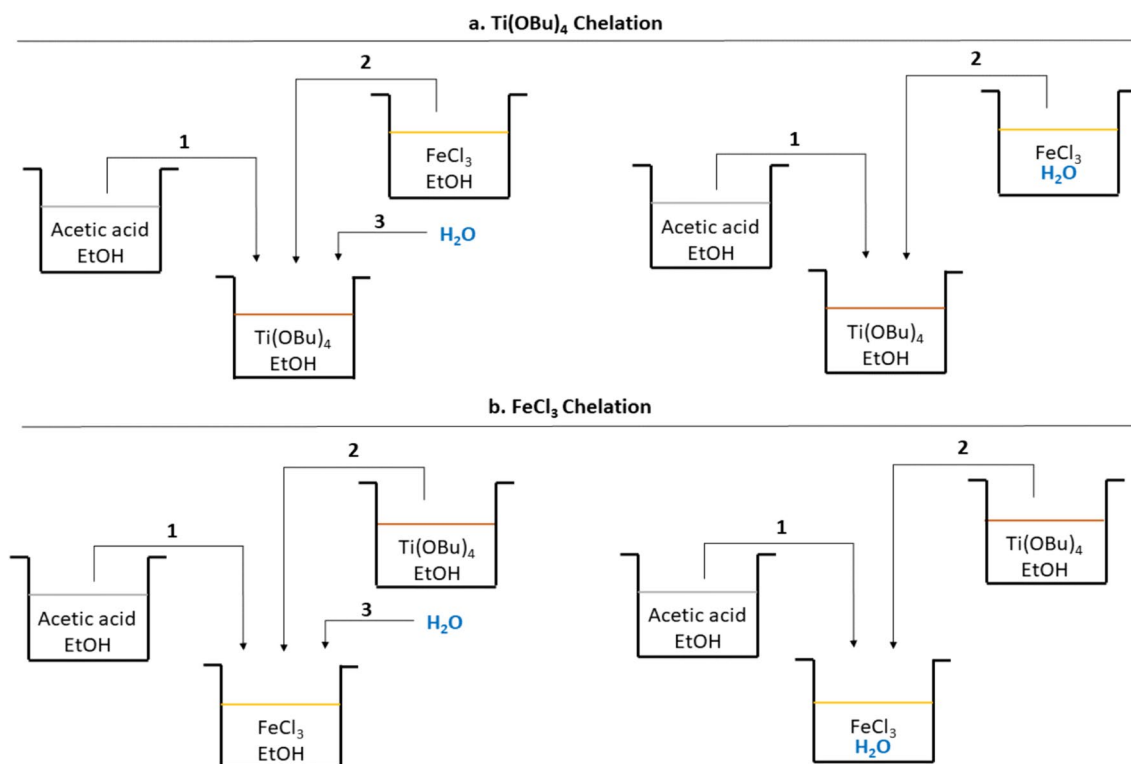


**Figure 1** Synthesis Routes with **a**  $\text{Ti}(\text{OBU})_4$  Chelation, molar ratio acetic acid/ $\text{Ti}(\text{OBU})_4$ : 1/1, 2/1 or 3/1 and **b**  $\text{FeCl}_3$  Chelation, molar ratio  $\text{FeCl}_3/\text{Ti}(\text{OBU})_4$ : 3/1, 6/1 or 9/1. Molar ratio  $\text{H}_2\text{O}/\text{Ti}(\text{OBU})_4$ : 4/1, EtOH: 15 mL.

In Routes III and IV, the mixing order was inverted aiming to chelate the other metal ion (Fe). Thus, the  $\text{FeCl}_3$  solution was taken as the core solution to which the acetic acid and  $\text{Ti}(\text{O}i\text{Bu})_4$  solutions were added subsequently. The values for molar ratios between acetic acid/ $\text{Ti}(\text{O}i\text{Bu})_4$ ,  $\text{FeCl}_3/\text{Ti}(\text{O}i\text{Bu})_4$ , and  $\text{H}_2\text{O}/\text{Ti}(\text{O}i\text{Bu})_4$  were the same as those used in Route I.

Each solution was prepared in beakers at room temperature and under 30 min of constant stirring prior to mixing. Once the precursor solutions were mixed, the reaction time was established at 1 h. The prepared sols were subjected to a 15-days aging period in complete darkness and at room temperature and pressure.

Following aging, the sols were dried in an oven at 100 °C for 24 h and the resulting xerogels were calcined at 550 °C for 3 h, with a heating rate of 5 °C  $\text{min}^{-1}$ , to obtain the materials. Note that the calcination conditions were selected based on preliminary experiments carried out to evaluate the effects of calcination temperature on the composition of iron titanate powders. In this regard, calcination was performed at 550 °C and 800 °C. The semiquantitative analyses of the XRD results for the synthesized materials calcined at 800 °C are shown in Table S1, and the comparison with the materials calcined at 550 °C showed that the latter temperature led to the predominant formation of iron titanate phases, and thus, 550 °C was chosen in this work as the calcination temperature based on both, the aforementioned experimental outcomes, as well as literature reports, in which it is also suggested a calcination time of 3 h to promote the formation of  $\text{Fe}_2\text{Ti}_3\text{O}_9$  [31]. Finally, the powders were manually grounded in an agate mortar, before and after calcination, to reduce their particle size.

## Physicochemical characterization

### *Characterization of the solutions during synthesis*

With the aim of analyzing the formation of chelation complexes in the reaction medium during the synthesis of iron titanate, Fourier-transform infrared spectroscopy (FTIR) was performed on the solutions obtained throughout the synthesis process. The spectra were acquired using an IRtracer-100 instrument

equipped with an ATR cell. Transmittance and absorbance profiles were analyzed using Labsolution IR software over a wavelength range of 400 to 4000 nm.

### *Characterization of the synthesized materials*

The powder materials obtained after calcination were characterized by X-ray diffraction (XRD) to identify the crystalline phases present in the samples and estimate their proportions. The XRD patterns were acquired using a Bruker D8 Advance powder diffractometer with DaVinci geometry (40 kV and 40 mA). Qualitative and semiquantitative analyses of the XRD patterns were performed in the software Diffraction EVA V.4.2. Nitrogen physisorption was carried out to determine the surface area of the powders. Adsorption isotherms were acquired using 3Flex-Micromeritics adsorption analyzer at 77 K and relative pressure between 0.0025 and 0.95. Data analysis was performed in the 3Flex-Micromeritics software V.4.03. Scanning electron microscopy—SEM, images were recorded to analyze the morphology of the synthesized materials. The micrographs were obtained using a Quanta FEG 650 Scanning Electron Microscope (high vacuum, 15 kV) with both secondary (SE) and backscattered (BSED) electrons detectors. UV–Vis Diffuse Reflectance Spectroscopy—DRS, recorded by a Shimadzu UB2600 UV–Vis Spectrometer (200–850 nm spectral range) was used to estimate the bandgap of the materials.

### *Evaluation of the photocatalytic activity*

The photocatalytic activity of the materials with the highest content of iron titanates (one for each synthesis route) was evaluated. For this, 0.5  $\text{mg mL}^{-1}$  of photocatalyst was suspended in 150 mL of a 200 ppm  $\text{CN}^-$  solution prepared from NaCN. The photocatalytic reaction was carried out in a 150 mL beaker. The reaction system was kept in the dark for 30 min to guarantee adsorption–desorption equilibrium, and afterward, the solution was irradiated for 3 h with two Phillips lamps (150 W each), placed equidistantly on each side of the beaker. Subsequently, the solutions were filtered to remove the photocatalyst and measure  $\text{CN}^-$  concentration. The concentration of  $\text{CN}^-$  was determined by potentiometric titration carried out in a Metrohm automatic titrator with  $\text{AgNO}_3$  0.017 N as titrant.

## Results and discussion

### Characterization of the solution

#### FTIR spectroscopy

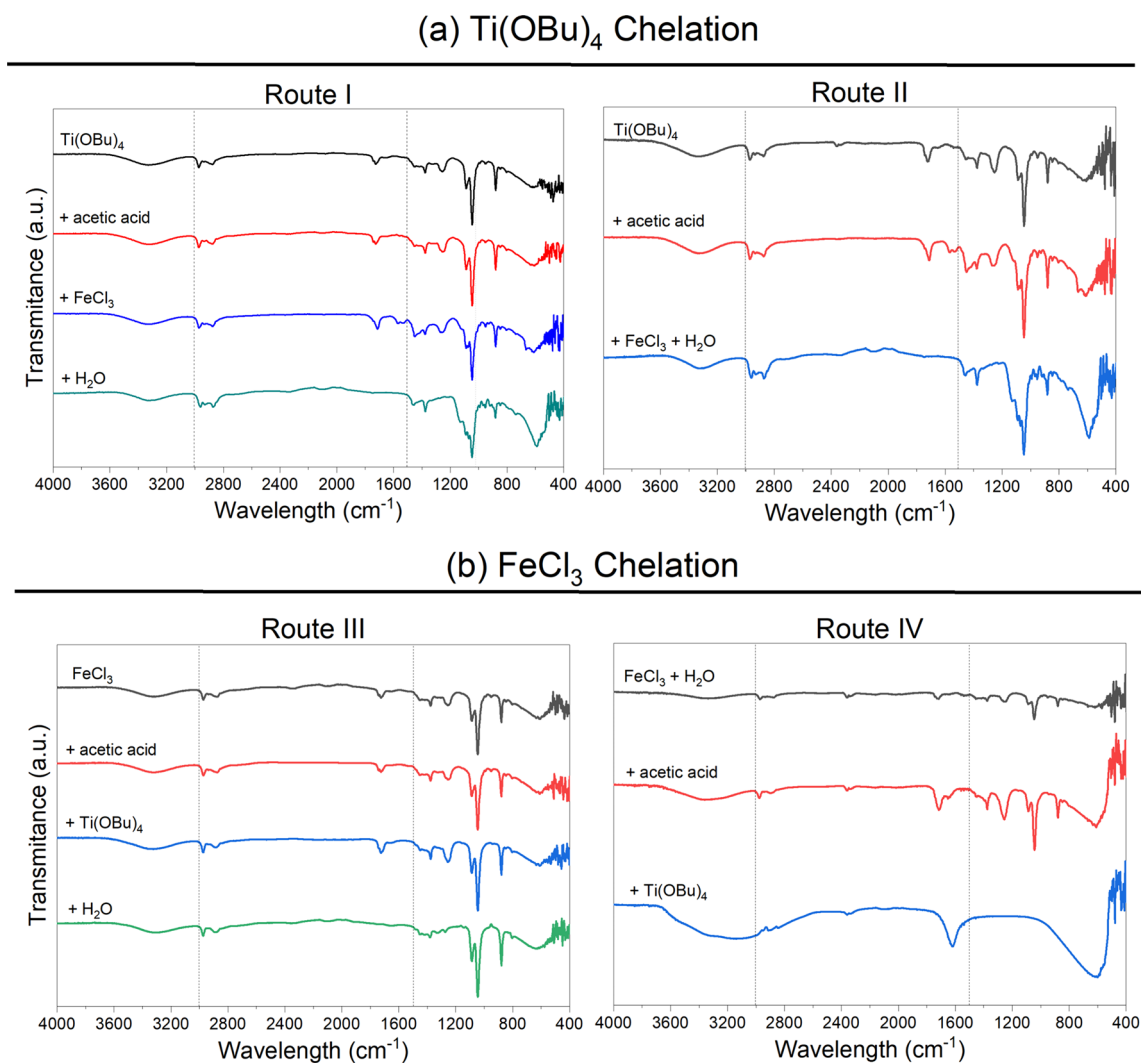
Fourier-transform infrared spectroscopy—FTIR, was performed for each step of each synthesis route in order to analyze the interactions that occur in the reaction medium and propose a reaction mechanism for the sol–gel synthesis of iron titanates using  $\text{Ti}(\text{OBU})_4$  and  $\text{FeCl}_3$  as metallic precursors, as well as to monitor the formation of metallic complexes by the action of acetic acid as a chelating agent.

As depicted in Fig. 2, all the spectra display a characteristic vibrational signal associated with the OH

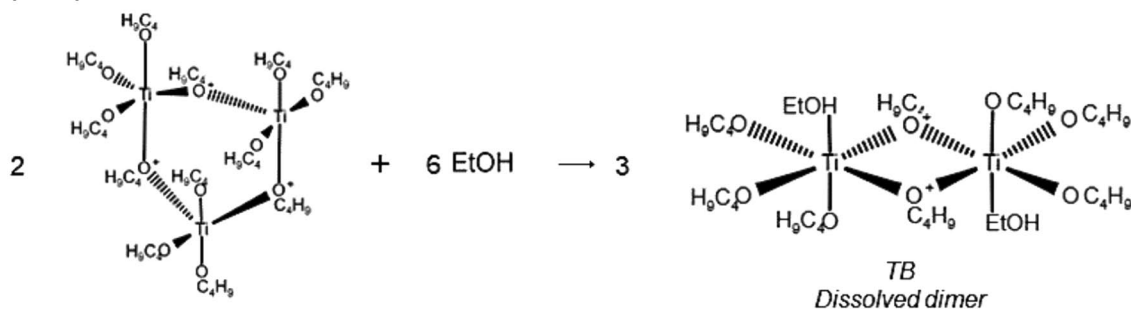
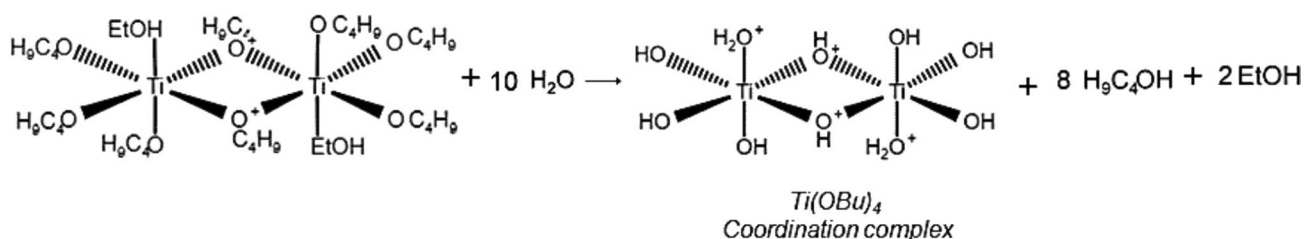
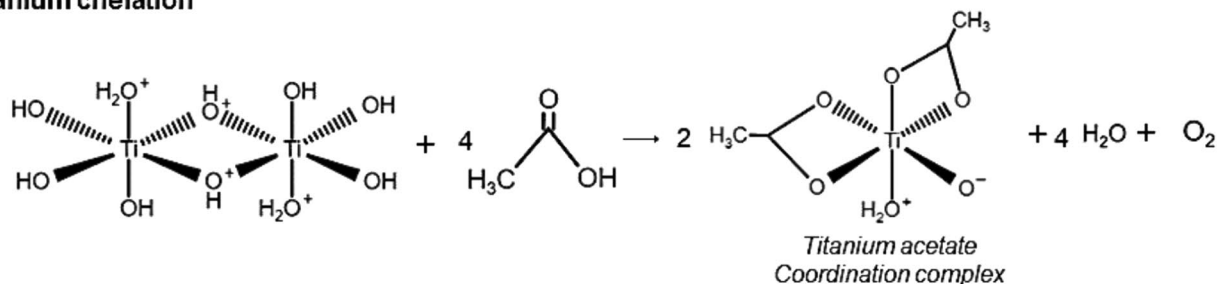
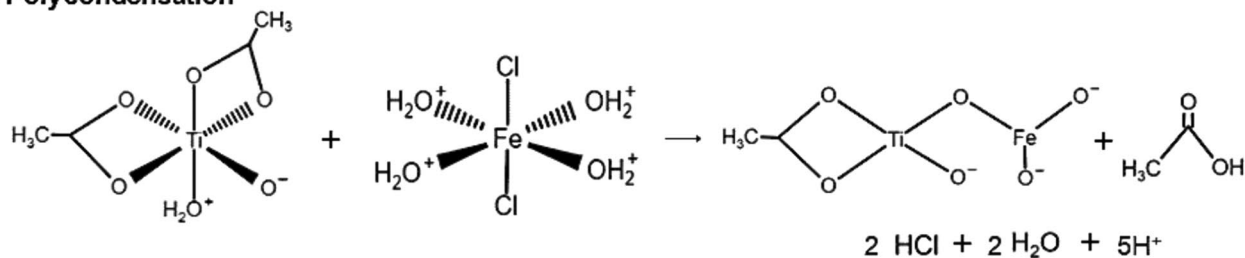
bond in the range of  $3230\text{--}3500\text{ cm}^{-1}$  [32], which indicates the presence of EtOH. Accordingly, it is noted that in Route IV this characteristic signal does not appear until the second synthesis step is carried out, *i.e.*, the addition of acetic acid dissolved in EtOH. This was expected as water is the solvent for the initial  $\text{FeCl}_3$  solution in Route IV.

Based on the FTIR spectroscopy results, reaction mechanisms between the chelating agent and each of the metal precursors [*i.e.*,  $\text{Ti}(\text{OBU})_4$  and  $\text{FeCl}_3$ ], are proposed as presented in Figs. 3 and 4, respectively.

When the chelated metal precursor reacts with water, the compound dissociates, forming coordination complexes (see Figs. 3b and 4a.). This reaction is the initial step in the synthesis process and can be evidenced in the spectra, with the appearance of strong



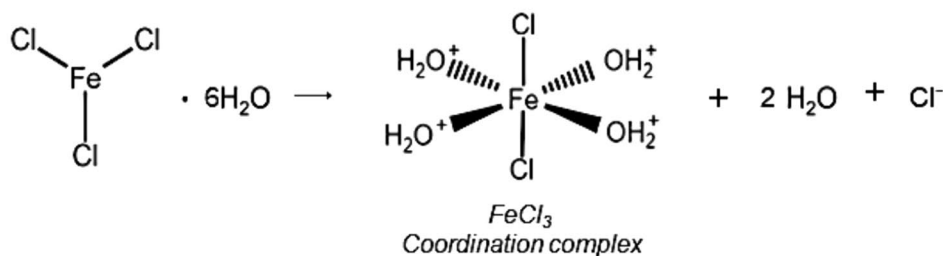
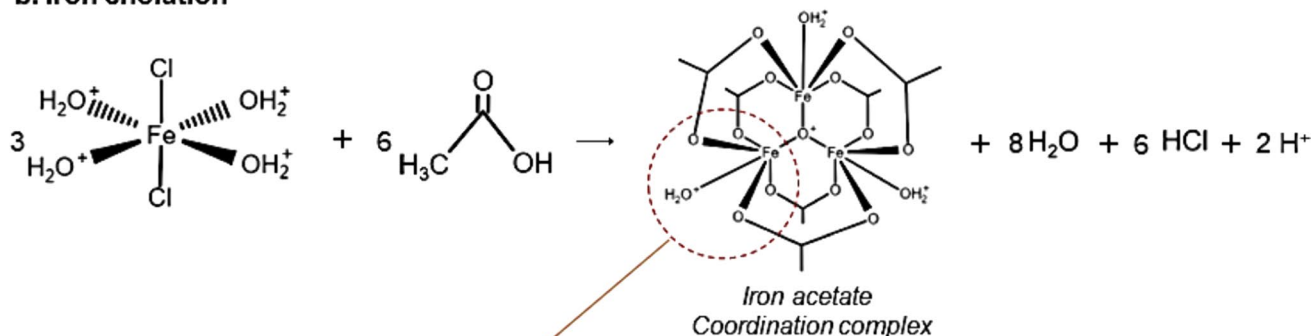
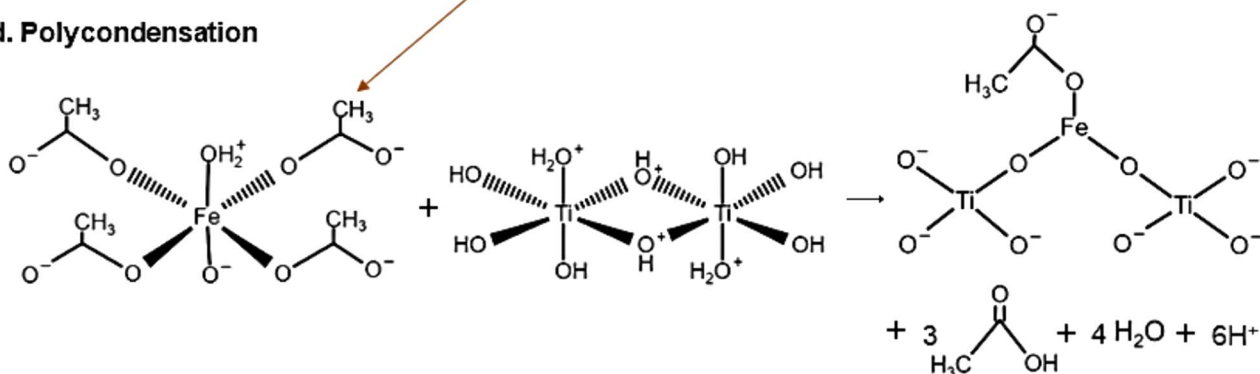
**Figure 2** FTIR spectra of every step followed in each synthesis route, molar ratio acetic acid/ $\text{Ti}(\text{OBU})_4$ : 3/1.

**a. Ti(OBu)<sub>4</sub> dissociation in EtOH****b. Ti(OBu)<sub>4</sub> hydrolysis****c. Titanium chelation****d. Polycondensation**

**Figure 3** Reaction mechanism when  $\text{Ti}(\text{OBu})_4$  is chelated with acetic acid [23, 38, 39].

signals located in the range of  $590\text{--}670\text{ cm}^{-1}$ , associated with  $\text{Ti}\text{--}\text{O}\text{--}\text{Ti}$  and  $\text{Fe}\text{--}\text{O}\text{--}\text{Fe}$  bonds [33]. It is important to note that the intensity of these peaks decreases as additional synthesis steps progress and other compounds are introduced into the mixture. This suggests the breaking of these bonds to result in the formation of acetate complexes or iron/titanium compounds, as it will be discussed below.

When acetic acid is introduced in the second step of synthesis, FTIR spectra from all routes show distinct signals at  $1250$  and  $1700\text{ cm}^{-1}$ . These signals correspond to the  $\text{C}\text{--}\text{O}$  bond stretching in acetic acid, as reported in the literature [34]. In both Route I and Route II, where the chelating agent is added to the core solution of  $\text{Ti}(\text{OBu})_4$ , these transmittance peaks exhibit a noticeable increase in intensity when compared to

**a. FeCl<sub>3</sub> dissociation****b. Iron chelation****c. TB hydrolysis (Figure 3→b)****d. Polycondensation**

**Figure 4** Reaction mechanism when FeCl<sub>3</sub> is chelated with acetic acid [23, 38, 39].

Routes III and IV. This increase is indicative of the formation of complexes between acetic acid and titanium butoxide, as documented by Perrin et al. [35], which supports the proposed titanium chelation step in the reaction mechanism (Fig. 3c).

On the other hand, in routes III and IV, two signals around 1650 and 1450 cm<sup>-1</sup>, with a band separation of 202 cm<sup>-1</sup>, are observed, supporting the formation of iron acetate complexes as proposed in Fig. 4b [36]. Notably, the low intensity of these peaks suggests ineffective iron chelation, consistent with prior research where the weak complex formation in systems involving iron chloride was proposed [37]. It is also important to consider that the concentration of the titanium

precursor is 3 times larger than the concentration of the iron precursor, which may favor titanium chelation over iron chelation.

Additionally, FTIR results revealed two signals corresponding to methyl rocking (*i.e.*, 1370–1376 cm<sup>-1</sup>) and scissoring (*i.e.*, 1444–1450 cm<sup>-1</sup>) vibrations, confirming the formation of acetate coordination complexes, according to the reported by Schubert and Weber et al.

These complexes must be subsequently decomposed to bind to the other metal precursor reagent [either Ti(OBu)<sub>4</sub> or FeCl<sub>3</sub>], finally leading to the formation of mixed oxides (Figs. 3d and 4d) [23, 38].

**Characterization of the mixed metal oxides**

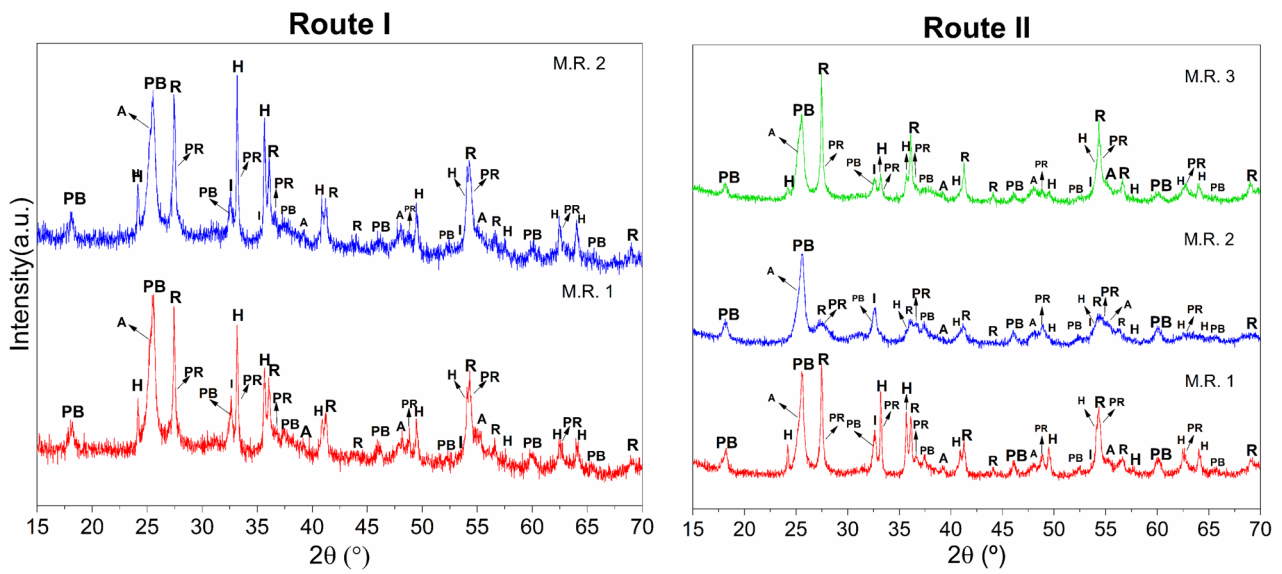
*X-ray diffraction*

The X-ray diffraction patterns of the materials synthesized through Routes I and II are shown in Fig. 5. The presence of pseudorutile ( $2\theta = 54.49$  and  $33.41^\circ$ , PDF 13-0326), pseudobrookite ( $2\theta = 25.52$  and  $32.49^\circ$ , PDF

41-1432), ilmenite ( $2\theta = 32.62$  and  $35.28^\circ$ , PDF 75-0519), rutile ( $2\theta = 27.44^\circ$  and  $36.07^\circ$ , PDF 73-1782), anatase ( $2\theta = 25.35$  and  $48.14^\circ$ , PDF 89-4921), and hematite ( $2\theta = 33.15$  and  $35.63^\circ$ , PDF 87-1164) is evidenced in all the materials.

In Route I, the XRD peaks for the materials synthesized with molar ratio acetic acid/Ti(OBu)<sub>4</sub> of 2 were noted to be slightly more intense and sharp as

(a) Ti(OBu)<sub>4</sub> Chelation



(b) FeCl<sub>3</sub> Chelation

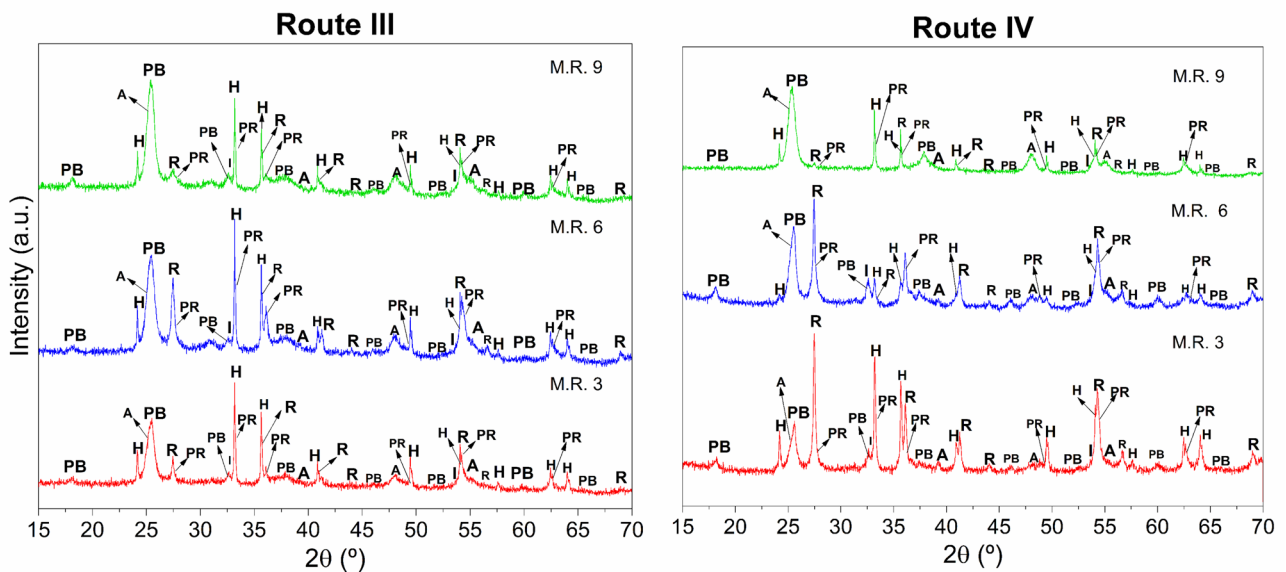


**Figure 5** XRD patterns of the materials synthesized **a** Ti(OBu)<sub>4</sub> Chelation, **b** FeCl<sub>3</sub> Chelation. (PB: pseudobrookite, H: hematite, R: rutile).



compared to the materials synthesized with molar ratio acetic acid/Ti(OBu)<sub>4</sub> of 1/1, which suggest a slight improvement in the crystallinity of the material when the concentration of chelating agent increases. However, increasing acetic acid/Ti(OBu)<sub>4</sub> molar ratio to 3/1 led to the formation of precipitates during the hydrolysis reaction, which interrupted the synthesis process. This can be attributed to the low chemical stability of the titanium butoxide (IV).

In contrast, for Route II, the characteristic peaks of the iron oxides and titanium oxides for the samples synthesized with molar ratio acetic acid/Ti(OBu)<sub>4</sub> of 2/1 exhibited low intensity, broad shape, and poor definition, unlike those synthesized with molar ratios acetic acid/Ti(OBu)<sub>4</sub> of 1/1 and 3/1. This infers that the production of iron titanates was favored over the production of oxides separately.

As demonstrated by the semiquantitative results in Table 1, the materials with the highest iron titanate content were obtained through Route II, which employed water as the solvent for the iron chloride solution, with 30% less solvent in the reaction medium compared to Route I. Under these conditions, the probability of the Ti(OBu)<sub>4</sub> to interact with the water molecules increases, allowing the hydrolysis of Ti(OBu)<sub>4</sub> (Fig. 3b) to take place more efficiently. This is crucial for the subsequent reaction to occur (Fig. 3c) where the chelating agent forms stable coordination complexes with metal ions in the titanium reagent. These complexes aid in controlling and reducing the hydrolysis rate, favoring polycondensation reactions, which lead to the synthesis of mixed oxides.

Another crucial factor that influences the iron titanate content in the materials is the concentration of the chelating agent. The semiquantitative results of the materials synthesized through Routes I and II show that the samples with the highest concentration of iron titanates were obtained using chelating agent in molar ratio acetic acid/Ti(OBu)<sub>4</sub> of 2/1, while those synthesized with molar ratio acetic acid/Ti(OBu)<sub>4</sub> of 3/1 exhibited the lowest content percentages. To understand this behavior, it is necessary to deep into the nature of the compounds involved.

The Ti<sup>4+</sup> cations have a coordination number of 5 in pure titanium butoxide and are bonded to one another through butoxy bridges, forming trimers. When the butoxide is diluted in nucleophilic solvents such as EtOH, titanium atoms reorganize to form dimers, due to the preference of Ti(OBu)<sub>4</sub> for an octahedral structure with coordination number of 6. This occurs by accepting free pairs of electrons from the nucleophilic ligands in their empty *d* orbitals (Fig. 6a) [40]. On the other hand, acetic acid is a bidentate carboxylic ligand; thus, it can chelate metal compounds by donating two electron pairs (Lewis's law) [41].

Therefore, titanium butoxide and acetic acid can bind in three different ways, depending on the molar ratio between them. When the chelating agent is added to the mixture in molar ratio acetic acid/Ti(OBu)<sub>4</sub> of 1/1 (Fig. 6a), the coordination complex is compelled to maintain its dimeric structure to conserve its coordination number and, thus, its stability. However, when the molar ratio is increased to 2/1 (Fig. 6b), the coordination complex of the titanium butoxide can keep its

**Table 1** Semiquantitative analysis results of the materials synthesized (Chelated metal precursor: Ti(OBu)<sub>4</sub> for Routes I and II; FeCl<sub>3</sub> for Routes III and IV)

Route	Molar ratio acetic acid/chelated metal precursor	Pseudorutile (wt.%)	Pseudobrookite (wt.%)	Ilmenite (wt.%)	TiO <sub>2</sub> (R) (wt.%)	TiO <sub>2</sub> (A) (wt.%)	Hematite (wt.%)	Titanates (wt.%)
I	1/1	23.4	21.7	6.4	19.4	10.9	18.1	51.5
	2/1	26.6	22.0	5.5	16.6	8.6	20.8	54.1
II	1/1	29.5	24.4	8.8	16.8	7.6	13.0	62.7
	2/1	29.8	45.3	1.8	5.3	15.0	2.6	76.9
	3/1	16.5	20.3	7.2	33.4	14.7	7.8	44.0
III	1/1	23.4	16.2	5.3	5.0	22.3	27.7	44.9
	2/1	30.9	10.0	2.7	15.0	13.1	28.3	43.6
	3/1	18.9	13.1	3.3	15.1	13.0	36.6	35.3
IV	1/1	34.3	10.5	3.4	26.1	21.4	4.3	48.2
	2/1	34.3	21.3	5.2	23.2	6.2	9.8	60.8
	3/1	18.1	9.0	1.4	1.0	36.8	32.7	28.5

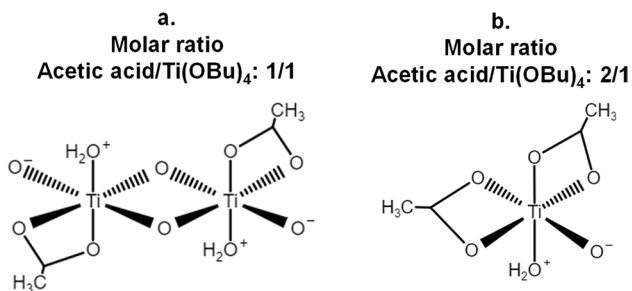


**Figure 6** Coordination complexes of  $\text{Ti}(\text{OBu})_4$  chelated with acetic acid **a** Molar ratio 1 and **b** Molar ratio 2 [23].

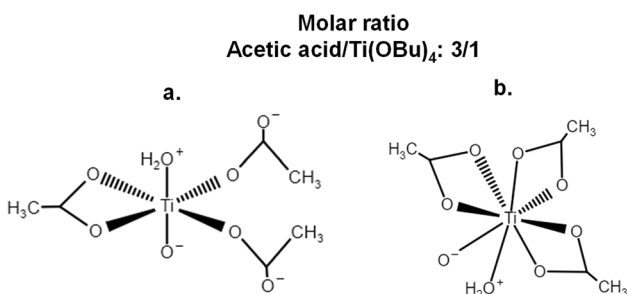


**Figure 7** Coordination complexes of  $\text{Ti}(\text{OBu})_4$  chelated with acetic acid, molar ratio acetic acid/ $\text{Ti}(\text{OBu})_4$ : 3/1, **a** monodentate bond, coordination number 6; and **b** bidentate bond, coordination number 8 [23].

coordination number in a more stable and less prone to precipitate monomeric structure [23].

Finally, when the molar ratio is increased to 3, two potential scenarios may happen: In the first scenario, only one molecule of the carboxylic acid binds through its two complexation sites, while the remaining two molecules are compelled to form monodentate bonds with the titanium butoxide (Fig. 7a). In the second scenario, the coordination number of titanium (IV) butoxide can increase to 8, accommodating all the electron pairs donated by the three carboxylic acid molecules (Fig. 7b). Both possibilities are unfavorable as they compromise the chemical stability of the system and its ability to control the kinetics of the sol–gel reactions, thereby increasing the probability of iron and titanium oxides forming separately. It is worth noting that at this molar ratio, it was impossible to synthesize any materials using Route I due to the precipitate formation during synthesis, providing direct evidence of the system's instability at high acetic acid concentrations in the medium [42].

The diffraction patterns of Routes III and IV are shown in Fig. 5(b), and the presence of pseudobrookite,

pseudorutile, rutile, anatase, and hematite was identified. The analysis of the XRD patterns exhibited the overlapping of some of the characteristic signals of iron titanates along with peaks ascribed to iron oxide (*i.e.*, hematite) and/or titanium oxide (*i.e.*, anatase and rutile); as a result, some of the peaks presented in the pattern can be decomposed into the individual contribution of two or more phases.

This behavior goes hand in hand with the previous FTIR analysis and can be further explained by analyzing the nature of the iron chelated compound. The strong magnetic bonds among the metal ions in the iron acetate hinder its decomposition, leading to the precipitation and posterior oxidation of these species [38]. This fact can be evidenced in the results, where, in general, there was an increase in the concentration of hematite in the materials as compared to Routes I and III.

Finally, in both Routes III and IV, it can be noted that the lowest content of iron titanates was obtained when using higher concentrations of acetic acid. This is owing to the tendency of  $\text{Fe}^{3+}$  ions to form iron hydroxides ( $\text{Fe}(\text{OH})_3$ ) at low pH values, which are later oxidized forming hematite in the calcination stage [43].

### Photocatalytic activity

The photocatalytic performance of the synthesized materials toward the removal of  $\text{CN}^-$  is exhibited in Fig. 8(a and b). As a reference, the performance of a  $\text{TiO}_2$  sample (Degussa P-25, 85% rutile/15% anatase) was evaluated and compared to the prepared samples.

As it can be noted, the overall removal of  $\text{CN}^-$  reached up to 20% ( $500 \text{ mg} \cdot \text{g}_{\text{cat}}^{-1}$ ). Nonetheless, it seems worth to analyze the two stages of the reaction separately. The first stage involves the removal of  $\text{CN}^-$  by its adsorption onto the surface of the catalyst during the initial 30 min in the dark. The subsequent stage involves irradiation of the system, considering that the adsorption/desorption equilibrium has already been reached, and thus, the removal of  $\text{CN}^-$  is solely attributed to photooxidation.

When  $\text{TiO}_2$  is used as photocatalysts, nearly 70% ( $\sim 350 \text{ mg} \cdot \text{g}_{\text{cat}}^{-1}$ ) of the total removal of  $\text{CN}^-$  is achieved purely by adsorption, an understandable result considering the physical properties of  $\text{TiO}_2$ , which is a porous material with high surface area ( $72\text{--}155 \text{ m}^2 \cdot \text{g}^{-1}$ ), thus conferring it the capacity to adhere a great number of molecules on its surface [44–46]. In contrast, the

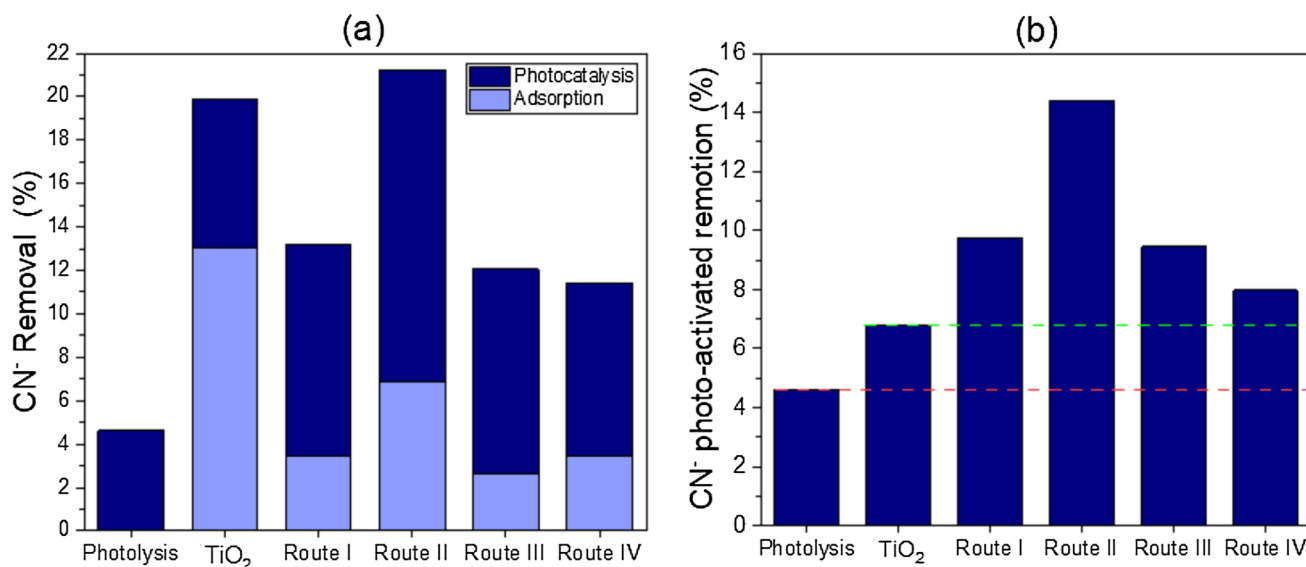


**Figure 8** **a** Overall remotion of CN<sup>-</sup>; **b** Remotion of CN<sup>-</sup> ascribed to photooxidation.

adsorption of CN<sup>-</sup> onto the synthesized materials does not exceed 7% of the total removal ( $\sim 200 \text{ mg} \cdot \text{g}_{\text{cat}}^{-1}$ ). This result can be explained by analyzing the morphology of the synthesized materials, which present a lower BET surface area ( $36.7 \pm 4.8 \text{ m}^2 \cdot \text{g}^{-1}$ ) compared to bare TiO<sub>2</sub>. Analyzing the type IV adsorption isotherms, with formation of type H3 hysteresis (Fig. 9a), and the SEM micrographs obtained (Fig. 9b), it can be concluded that the powders consist of agglomerated mesoporous nanometric particles [47, 48]. It is important to note that SEM analysis focused exclusively on the material synthesized via route II, in which the highest concentration of iron titanates was obtained. The analysis of the nitrogen physisorption isotherms and the estimated BET surface area for all samples showed similar surface area values across the materials synthesized via different routes. This similarity suggests that the mixing order had minimal influence on the surface morphology of the materials. Therefore, the sample obtained through Route II provided a representative understanding of the general morphology of all synthesized materials.

On the other hand, Fig. 8(b) exhibits the results for the photoactivated removal of CN<sup>-</sup>. It can be noted that all the materials exceeded the removal attributed to the exclusive incidence of visible light irradiation in the absence of catalyst (photolysis), proving that the synthesized materials exhibited photocatalytic activity. Interestingly, it is also noted that the synthesized

titanates could photooxidize 65% more CN<sup>-</sup> compared with TiO<sub>2</sub>, despite possessing lower surface area.

Additional physicochemical analyses were performed to comprehensively understand these results. The bandgap energy values ( $E_g$ ) of the synthesized materials were estimated by applying the Kubelka–Munk function to the UV–Vis DRS data, as depicted in Fig. 9(c). The values of  $E_g$  for the synthesized materials range from 2.31 to 2.90 eV, which indicates that the samples could be activated under the incidence of visible light irradiation, exhibiting enhanced photoactivity compared to bare TiO<sub>2</sub>.

With the aim of analyzing in greater depth the influence of iron titanates on the photoremoval of CN<sup>-</sup>, a mathematical analysis was carried out using multivariate linear regression (Eq. 1), where  $W_i$  is the normalized weight fraction of the crystalline phase  $i$  (*i.e.*, iron titanates, rutile, hematite, and anatase) and  $\omega_i$  stands for the relative contribution of the correspondent phase  $i$  to the normalized final photocatalytic removal of CN<sup>-</sup>.

The normalization of the variables was carried out by following the Min–Max scaling method [49]. As it depicted in Eq. 2, each value of  $w_i$  (weight fraction of crystalline phase  $i$  in the material) was transformed to  $W_i$ , in such a way that the coefficients of each variable were in a range of values from 0 to 1, representing the materials with lower and higher content of phase  $i$ , respectively. This data treatment was also realized

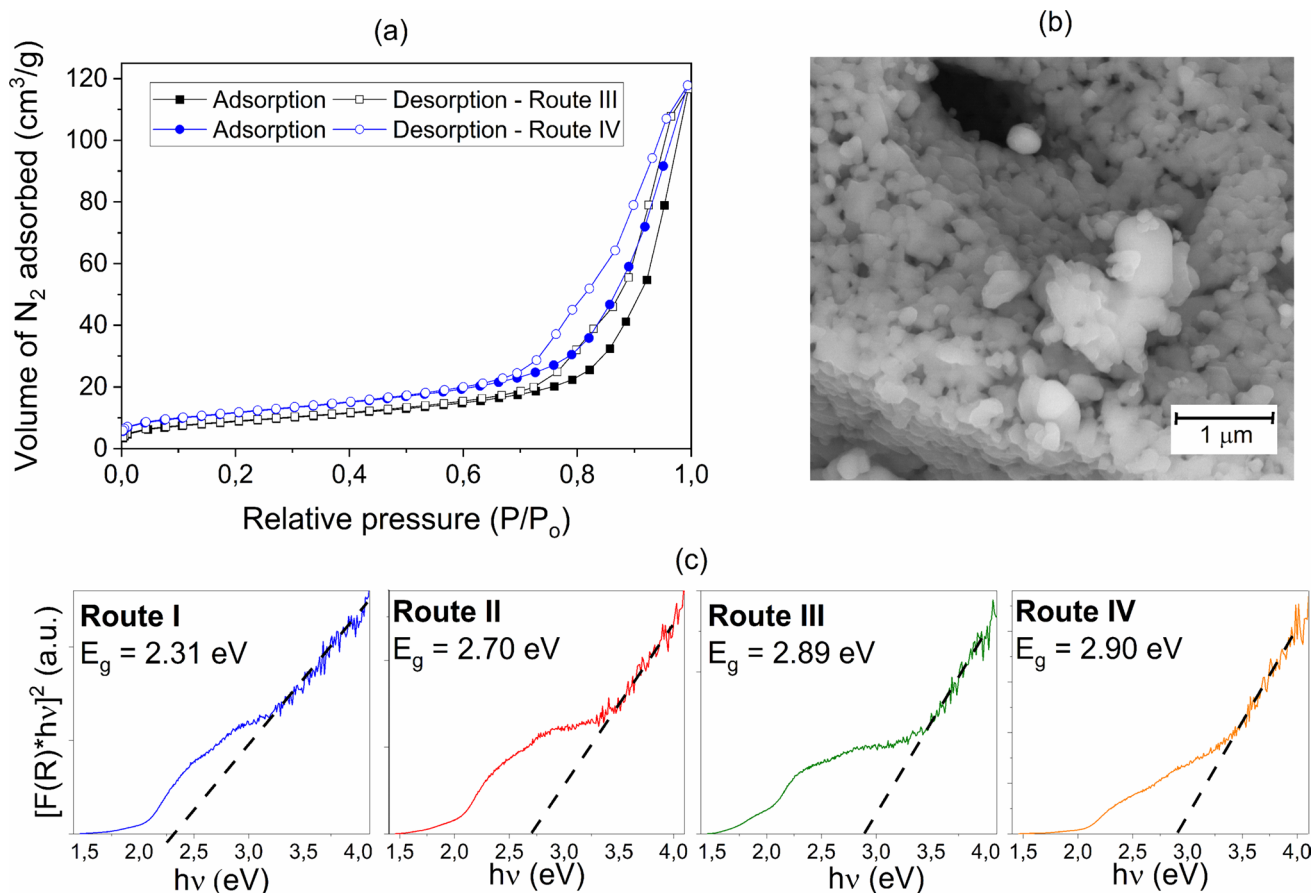


**Figure 9** **a** Isotherms of N<sub>2</sub> physisorption for the samples synthesized through routes III and IV; **b** SEM micrographs of the sample synthesized through route II; **c** E<sub>g</sub> estimation by Kubelka–Munk function.

**Table 2** Parameters of the multivariable system to assess the influence of each crystalline phase on photocatalytic removal of CN<sup>-</sup>

Sample	W <sub>Titanates</sub>	W <sub>Rutile</sub>	W <sub>Hematite</sub>	W <sub>Anatase</sub>	CN <sup>-</sup> <sub>Removal</sub>
Route I	0.288	0.637	0.725	0.000	0.302
Route II	1.000	0.016	0.000	0.467	1.000
Route III	0.000	0.000	1.000	1.000	0.267
Route IV	0.497	1.000	0.143	0.088	0.000

for the dependent variable (percentage of cyanide removed photocatalytically).

Table 2 summarizes the values of normalized  $w_i$  and  $CN^-_{Removal}$  for each route.

$$(W_{Titanates} * \omega_T) + (W_{Rutile} * \omega_R) + (W_{Hematite} * \omega_H) + (W_{Anatase} * \omega_A) = CN^-_{Removal} \tag{1}$$

$$W_i = \frac{w_i - w_{min}}{w_{max} - w_{min}} \tag{2}$$

The resultant 4 × 4 system of equations was solved using MATLAB, R2023b version, and the values of  $w_i$  obtained were:  $\omega_{Titanates} = 1.12$ ,  $\omega_{Hematite} = 0.51$ ,  $\omega_{Anatase} = 0.24$ , and  $\omega_{Rutile} = -0.61$ . From these results, it is deduced that iron titanates were the phase with greatest influence on the photocatalytic performance of the materials. Furthermore, it is observed that hematite, a phase that also contains Fe in its crystalline structure, made the second largest contribution. In fact, the contribution of hematite is also observed in the diffuse reflectance spectra of the samples, where signals in the range of 1.9 to 2.2 eV are present

(Fig. 9c). This range is consistent with the bandgap ( $E_g$ ) reported for hematite [50] and enhances the ability of the material to absorb a higher percentage of visible light, consequently increasing the generation of electron–hole pairs and improving photocatalytic activity.

Consequently,  $\text{TiO}_2(\text{A})$  and  $\text{TiO}_2(\text{R})$  phases, with wider bandgap values [51, 52], contributed to a lesser extent to the photocatalytic activity. In the case of rutile, a negative value of  $\omega$  was obtained when solving the equations system, indicating a counterproductive effect on the photocatalytic performance of the synthesized materials caused by its presence. Conversely, the positive impact of anatase can be primarily attributed to its ability to generate free hydroxyl radicals ( $\text{OH}^\bullet$ ), facilitating the oxidation of both surface-bound and free  $\text{CN}^-$  molecules in the solution [53].

In addition, an analysis of the photocatalytic performance in relation with the physicochemical properties of the samples showed an inverse relation between the weight percentage of pseudorutile contained in the synthesized materials and their photocatalytic activity toward the degradation of  $\text{CN}^-$ . This can be explained considering some scientific papers that refer to this iron titanate as an impurity that negatively affects the photocatalytic properties of ilmenite [54], owing to its low physicochemical stability. Thus, samples with larger amount of pseudorutile can exhibit lower stability and, therefore, accomplish fewer photodegradation.

## Conclusions

Nanomaterials containing iron titanates [pseudobrookite ( $\text{Fe}_2\text{TiO}_5$ ), pseudorutile ( $\text{Fe}_2\text{Ti}_3\text{O}_9$ ), and ilmenite ( $\text{FeTiO}_3$ )] and metal oxides [anatase ( $\text{TiO}_2(\text{A})$ ), rutile ( $\text{TiO}_2(\text{R})$ ), and hematite ( $\text{FeO}_3$ )] were synthesized using the sol–gel method and employing acetic acid as chelating agent. The concentration of the chelating agent plays an important role in the determination of the molecular structure and the coordination complexes stability, influencing the ability of the chelating agent to control the kinetics of the sol–gel method reactions and favoring the formation of mixed oxides above the formation of simple oxides. These findings were supported by the proposal of reaction mechanisms. The synthesized materials were able to photooxidize a higher percentage of  $\text{CN}^-$  than a  $\text{TiO}_2$  sample. Enhanced photooxidation outcomes can be achieved through the

implementation of particle size treatment to increase the surface area of the synthesized materials. The iron titanates content positioned the energy bandgap within the range of 2.31 to 2.90 eV, facilitating the activation of the materials under visible light and enabling the degradation of  $\text{CN}^-$ . A mathematical analysis confirmed that iron titanates were the crystalline phase that most influenced the photocatalytic performance of the synthesized materials.

## Acknowledgements

This paper is dedicated in memoriam to Prof. Ricardo Gómez (1944–2023), Universidad Autónoma Metropolitana-Iztapalapa (México), pioneer in the development of sol-gel catalysts: T. López and R. Gómez, R. (1994). Catalyst Doped Sol-Gel Materials. in: L.C. Klein (Ed.), Sol-Gel Optics: Processing and Applications. The Kluwer International Series in Engineering and Computer Science (SECS, Vol. 259). Kluwer, Boston, MA. pp. 345–371, [https://doi.org/10.1007/978-1-4615-2750-3\\_16](https://doi.org/10.1007/978-1-4615-2750-3_16). The authors acknowledge the support of Professor J.A. Henao-Martínez from the X-ray Laboratory (Universidad Industrial de Santander—UIS, Colombia) for his collaboration with XRD data, the Laboratory of Microscopy at UIS, for the assistance with the SEM-EDS recording, and the Centro de Investigación en Catálisis—CICAT at UIS, for the cooperation with the nitrogen physisorption measurements. The authors also acknowledge to the Fundación para la Promoción de la Investigación y la Tecnología, Banco de la República (Colombia), for the partial funding provided through the research project No. 4.184. D.M. Cañas-Martínez acknowledges the School of Chemical Engineering for the financial support through the Doctoral Scholarship assigned with the contract No. 69 of 2018. J. Vazquez-Samperio acknowledges the Consejo Nacional de Ciencia y Tecnología—CONACYT for the postdoctoral position, and the Secretaría de Educación, Ciencia, Tecnología e Innovación de la Ciudad de México—SECTEI for financial support provided through project 094/2023.

## Author contribution

SC-M contributed to conceptualization, methodology, validation, formal analysis, investigation, writing—original draft, writing—review and editing,

visualization, and project administration. ICO-R was involved in conceptualization, methodology, validation, formal analysis, investigation, writing—original draft, writing—review and editing, and visualization. DMC-M contributed to conceptualization, methodology, validation, formal analysis, investigation, writing—original draft, writing—review and editing, visualization, and project administration. JV-S was involved in methodology, formal analysis, resources, and writing—review and editing. JAP-A contributed to conceptualization, methodology, formal analysis, resources, writing—review and editing, supervision, project administration, and funding acquisition.

## Funding

Open Access funding provided by Colombia Consortium.

## Declarations

**Conflict of interest** The authors declare that they have no conflicts of financial interest or personal relationships that could have influenced the work presented in this article.

**Data availability** There are no additional data to access derived from the research.

**Ethical approval** No experiments involving human tissue or human derived samples were carried out. The ethical aspects of this research were evaluated and approved by the ethics committee at Universidad Industrial de Santander: Comité de Ética en Investigación Científica, CEINCI-UIS.

**Supplementary Information** The online version contains supplementary material available at <https://doi.org/10.1007/s10853-024-09940-7>.

**Open Access** This article is licensed under a Creative Commons Attribution 4.0 International License, which permits use, sharing, adaptation, distribution and reproduction in any medium or format, as long as you give appropriate credit to the original author(s) and the source, provide a link to the Creative Commons licence, and indicate if changes were made.

The images or other third party material in this article are included in the article's Creative Commons licence, unless indicated otherwise in a credit line to the material. If material is not included in the article's Creative Commons licence and your intended use is not permitted by statutory regulation or exceeds the permitted use, you will need to obtain permission directly from the copyright holder. To view a copy of this licence, visit <http://creativecommons.org/licenses/by/4.0/>.

## References

- [1] Koe WS, Lee JW, Chong WC et al (2020) An overview of photocatalytic degradation: photocatalysts, mechanisms, and development of photocatalytic membrane. *Environ Sci Pollut Res* 27:2522–2565
- [2] Ochoa Rodríguez PA, Pecchi GA, Casuscelli SG et al (2019) A simple synthesis way to obtain iron-doped TiO<sub>2</sub> nanoparticles as photocatalytic surfaces. *Chem Phys Lett* 732:136643. <https://doi.org/10.1016/j.cplett.2019.136643>
- [3] Wang CY, Bahnemann DW, Dohrmann JK (2000) A novel preparation of iron-doped TiO<sub>2</sub> nanoparticles with enhanced photocatalytic activity. *Chem Commun* 16:1539–1540. <https://doi.org/10.1039/b002988m>
- [4] Dharma HNC, Jaafar J, Widiastuti N et al (2022) A review of titanium dioxide (TiO<sub>2</sub>)-based photocatalyst for oilfield-produced water treatment. *Membranes (Basel)* 12:345. <https://doi.org/10.3390/membranes12030345>
- [5] Dong H, Zeng G, Tang L et al (2015) An overview on limitations of TiO<sub>2</sub>-based particles for photocatalytic degradation of organic pollutants and the corresponding countermeasures. *Water Res* 79:128–146
- [6] Ghorbanpour M, Feizi A (2019) Iron-doped TiO<sub>2</sub> catalysts with photocatalytic activity. *J Water Environ Nanotechnol* 4:60–66. <https://doi.org/10.22090/jwent.2019.01.006>
- [7] Chen YH (2011) Synthesis, characterization and dye adsorption of ilmenite nanoparticles. *J Non Cryst Solids* 357:136–139. <https://doi.org/10.1016/j.jnoncrysol.2010.09.070>
- [8] Sohail M, Tahir N, Rubab A et al (2020) Facile synthesis of iron-titanate nanocomposite as a sustainable material for selective amination of substituted nitro-arenes. *Catalysts* 10:1–12. <https://doi.org/10.3390/catal10080871>
- [9] Ovsyannikov SV, Tsirlin AA, Korobeynikov IV et al (2021) Synthesis of ilmenite-type ε-Mn<sub>2</sub>O<sub>3</sub> and its properties. *Inorg Chem* 60:13348–13358. <https://doi.org/10.1021/acs.inorgchem.1c01666>

- [10] Trang NTT, Khang DM, Dung DD et al (2021) Synthesis of ilmenite  $\text{NiTiO}_3$  rods and effect of pH on Rhodamine B textile dye degradation under LED visible-light irradiation. *J Electron Mater* 50:7188–7197. <https://doi.org/10.1007/s11664-021-09260-5>
- [11] Fauzi A, Lalasari LH, Ofyan NS et al (2022) Synthesis of titanium dioxide nanotube derived from ilmenite mineral through post-hydrothermal treatment and its photocatalytic performance. *Eastern-Eur J Enterp Technol* 2:15–29. <https://doi.org/10.15587/1729-4061.2022.255145>
- [12] Sun X, Li Y (2003) Synthesis and characterization of ion-exchangeable titanate nanotubes. *Chem Eur J* 9:2229–2238. <https://doi.org/10.1002/chem.200204394>
- [13] Sharma YK, Kharkwal M, Uma S, Nagarajan R (2009) Synthesis and characterization of titanates of the formula  $\text{MTiO}_3$  ( $M = \text{Mn, Fe, Co, Ni}$  and  $\text{Cd}$ ) by co-precipitation of mixed metal oxalates. *Polyhedron* 28:579–585. <https://doi.org/10.1016/j.poly.2008.11.056>
- [14] Mona J, Kale SN, Gaikwad AB et al (2006) Chemical methods to synthesize  $\text{FeTiO}_3$  powders. *Mater Lett* 60:1425–1427. <https://doi.org/10.1016/j.matlet.2005.11.041>
- [15] Zarazúa-Morín ME, Torres-Martínez LM, Moctezuma E et al (2016) Synthesis, characterization, and catalytic activity of  $\text{FeTiO}_3/\text{TiO}_2$  for photodegradation of organic pollutants with visible light. *Res Chem Intermed* 42:1029–1043. <https://doi.org/10.1007/s11164-015-2071-9>
- [16] Mahmoud MHH, Hessien MM, Alhadhrani A, Gobouri AA (2019) Physicochemical properties of pseudobrookite  $\text{Fe}_2\text{TiO}_5$  synthesized from ilmenite ore by co-precipitation route. *Physicochem Probl Miner Process* 55:290–300. <https://doi.org/10.5277/ppmp18131>
- [17] Temple AK (1966) Alteration of ilmenite. *Econ Geol* 61:695–714
- [18] Jacobs J, Marques MAL, Wang HC et al (2021) Structure, magnetism, and thermal stability of  $\text{La}_2\text{NiO}_{2.5}\text{F}_3$ : a ruddlesden-popper oxyfluoride crystallizing in space group  $P4_2/nm$ . *Inorg Chem* 60:13646–13657. <https://doi.org/10.1021/acs.inorgchem.1c01957>
- [19] Boumezoued A, Guergouri K, Barille R et al (2021) Synthesis and characterization of ZnO-based nanopowders: study of the effect of sintering temperature on the performance of ZnO– $\text{Bi}_2\text{O}_3$  varistors. *J Mater Sci Mater Electron* 32:3125–3139. <https://doi.org/10.1007/s10854-020-05062-3>
- [20] Zang Y, Xiao G, Ding D et al (2021) Synthesis of in-situ high-content carbon-containing calcium aluminate cement and its effect on the properties of  $\text{Al}_2\text{O}_3$ – $\text{SiC}$ – $\text{C}$  castables. *J Asian Ceram Soc* 9:549–558. <https://doi.org/10.1080/21870764.2021.1902072>
- [21] Dislich H, Hinz P (1982) History and principles of the sol-gel process, and some new multicomponent oxide coatings. *J Non-Cryst Solids* 48:11–16
- [22] Dislich H (1971) New routes to multicomponent oxide glasses. *Angew Chem* 10:363–434
- [23] Schubert U (2005) Chemical modification of titanium alkoxides for sol-gel processing. *J Mater Chem* 15:3701–3715. <https://doi.org/10.1039/b504269k>
- [24] Khaleel A (2009) Sol-gel synthesis, characterization, and catalytic activity of Fe(III) titanates. *Colloids Surf A Physicochem Eng Asp* 346:130–137. <https://doi.org/10.1016/j.colsurfa.2009.06.003>
- [25] Bokov D, Turki Jalil A, Chupradit S, Suksatan W, Javed M, Shewael IH, Valiev GH, Kianfar E (2021) Nanomaterial by Sol-Gel method: synthesis and application. *Adv. Mater. Sci. Eng* 2021:5102014–5102035. <https://doi.org/10.1155/2021/5102014>
- [26] Osman N, Abdullah NA, Hasan S (2014) Chelating agent role in synthesizing cerate-zirconate powder by a sol-gel method. *Adv Mater Res* 896:112–115
- [27] Saravanakumar B, Anusiya A, Rani BJ et al (2018) Role of different chelating agent in synthesis of copper doped tin oxide ( $\text{Cu-SnO}_2$ ) nanoparticles. In: AIP conference proceedings. American Institute of Physics Inc.
- [28] Guzmán AM, Fernández AM, Franco Y et al (2007) Estudio de las reacciones de hidrólisis y condensación del titanio en presencia. *Rev Acad Colomb Cienc XXXI*
- [29] Ponmani S, Vishnupriya R, Rajeshwari T, Prabhu MR (2018) Preparation and characterization of pseudobrookite ( $\text{Fe}_2\text{TiO}_5$ ) nano composite for fuel cell applications. *International Journal of Advance Engineering and Research Development International Conference on Momentous Role of Nanomaterials in Renewable Energy Devices* 5:1–5
- [30] Chen J, Lin J, Chen J, Wang J (2019) Effect of small molecular organic acids on the structure and catalytic performance of sol-gel prepared cobalt cerium oxides towards toluene combustion. *Catalysts* 9:483. <https://doi.org/10.3390/catal9050483>
- [31] Zhang G, Ostrovski O (2002) Effect of preoxidation and sintering on properties of ilmenite concentrates. *Int J Miner Process* 64:201–218
- [32] Mudalip SKA, BakarMohd RA, Adam F, Jamal P (2013) Structures and hydrogen bonding recognition of mefenamic acid form I crystals in mefenamic acid/ethanol solution. *Int J Chem Eng Appl* 4:124–128. <https://doi.org/10.7763/ijcea.2013.v4.277>
- [33] Solano Pizarro RA, Herrera Barros AP (2020) Cypermethrin elimination using Fe– $\text{TiO}_2$  nanoparticles supported on coconut palm spathe in a solar flat plate photoreactor.

- Adv Compos Lett 29:1–13. <https://doi.org/10.1177/2633366X20906164>
- [34] Banno M, Ohta K, Tominaga K (2008) Ultrafast dynamics of the carbonyl stretching vibration in acetic acid in aqueous solution studied by sub-picosecond infrared spectroscopy. *J Phys Chem A* 112:4170–4175. <https://doi.org/10.1021/jp076920m>
- [35] Perrin FX, Nguyen V, Vernet JL (2003) FT-IR spectroscopy of acid-modified titanium alkoxides: investigations on the nature of carboxylate coordination and degree of complexation. *J. Sol-Gel Sci. Technol* 28: 205-215. <https://doi.org/10.1023/A:1026081100860>
- [36] Muthukumar K, Kaleekkal NJ, Shanthana D et al (2019) Tuning the morphology of PVDF membranes using inorganic clusters for oil/water separation. *J Appl Polym Sci* 136(24) 1–10. <https://doi.org/10.1002/app.4>
- [37] Persson I (2018) Ferric chloride complexes in aqueous solution: An EXAFS study. *J. Solut. Chem* 47(5):797-805. <https://doi.org/10.1007/s10953-018-0756-6>
- [38] Weber B, Betz R, Bauer W, Schlamp S (2011) Crystal structure of iron(II) acetate. *Z Anorg Allg Chem* 637:102–107. <https://doi.org/10.1002/zaac.201000274>
- [39] Burgess J, Twigg MV (2006) Iron: inorganic & coordination chemistry based in part on the article iron: inorganic & coordination chemistry by Hawker PN & Twigg MV which appeared in the encyclopedia of inorganic chemistry, First Edition. In: *Encyclopedia of inorganic chemistry*. Wiley
- [40] Barboux-Doeuff S, Sanchez C (1994) Synthesis and characterization of titanium oxide-based gels synthesized from acetate modified titanium butoxide precursors. *Mater Res Bull* 29:1–13
- [41] Assi H, Mouchaham G, Steunou N et al (2017) Titanium coordination compounds: from discrete metal complexes to metal-organic frameworks. *Chem Soc Rev* 46:3431–3452
- [42] Prathan A, Sanglao J, Wang T et al (2020) Controlled structure and growth mechanism behind hydrothermal growth of TiO<sub>2</sub> nanorods. *Sci Rep* 10:8065. <https://doi.org/10.1038/s41598-020-64510-6>
- [43] Monhemius AJ (1977) Precipitation diagrams for metal hydroxides sulphates, arsenates and phosphates. *Trans Inst Min Metall* 86:C202–C206
- [44] Andrade-Guel M, Díaz-Jiménez L, Cortés-Hernández D et al (2018) Microwave assisted sol–gel synthesis of titaniumdioxide using hydrochloric and acetic acid ascatalysts. *Bol Soc Esp Ceram Vidrio* 58:171–177. <https://doi.org/10.1016/j.bsecv.2018.10.005>
- [45] Fajriati I, Mudasir M, Wahyuni ET (2019) Adsorption and photodegradation of cationic and anionic dyes by TiO<sub>2</sub>-chitosan nanocomposite. *Indones J Chem* 19:441–453
- [46] Khemthong P, Photai P, Grisdanurak N (2013) Structural properties of CuO/TiO<sub>2</sub> nanorod in relation to their catalytic activity for simultaneous hydrogen production under solar light. *Int J Hydrog Energy* 38:15992–16001. <https://doi.org/10.1016/j.ijhydene.2013.10.065>
- [47] Xue M, Chen H, Ge J, Shen J (2010) Preparation and characterization of thermally stable high surface area mesoporous vanadium oxides. *Microporous Mesoporous Mater* 131:37–44. <https://doi.org/10.1016/j.micromeso.2009.11.038>
- [48] Chang SS, Clair B, Ruelle J et al (2009) Mesoporosity as a new parameter for understanding tension stress generation in trees. *J Exp Bot* 60:3023–3030. <https://doi.org/10.1093/jxb/erp133>
- [49] Krishna SG, Kumar sahu K (2015) Normalization: a pre-processing stage. *IARJSET* 2:20-22. <https://doi.org/10.17148/IARJSET.2015.2305>
- [50] Li J, Chu D (2018) Energy band engineering of metal oxide for enhanced visible light absorption. In: *Multifunctional photocatalytic materials for energy*. Woodhead Publishing in Materials 49-78. <https://doi.org/10.1016/B978-0-08-101977-1.00005-3>.
- [51] Dette C, Pérez-Osorio MA, Kley CS et al (2014) TiO<sub>2</sub> anatase with a bandgap in the visible region. *Nano Lett* 14:6533–6538. <https://doi.org/10.1021/nl503131s>
- [52] Nosaka Y, Nosaka AY (2016) Reconsideration of intrinsic band alignments within anatase and rutile TiO<sub>2</sub>. *J Phys Chem Lett* 7:431–434
- [53] Odling G, Robertson N (2015) Why is anatase a better photocatalyst than rutile? The importance of free hydroxyl radicals. *Chemsuschem* 8:1838–1840
- [54] Spencer W, Ibana D, Singh P, Nikoloski AN (2022) Effect of ilmenite properties on synthetic rutile quality. *Miner Eng* 177:107365. <https://doi.org/10.1016/J.MINENG.2021.107365>

**Publisher's Note** Springer Nature remains neutral with regard to jurisdictional claims in published maps and institutional affiliations.